American Mineralogist, Volume 82, pages 858–869, 1997

Electron-irradiation-induced phase segregation in crystalline and amorphous apatite: A TEM study

A. MELDRUM, L.M. WANG,* AND R.C. EWING*

Department of Earth and Planetary Sciences, University of New Mexico, Albuquerque, New Mexico 87131-1116, U.S.A.

ABSTRACT

Single crystals of natural F-rich apatite and 800 keV Kr^{2+} ion-beam–amorphized apatite were irradiated by an electron beam in a transmission electron microscope over a range of beam energies and beam currents. Irradiation of crystalline apatite using a high current density (16 A/cm^2) caused the precipitation of cubic CaO from the crystalline apatite matrix. Using a lower beam current (1.6 A/cm^2), the formation of nanometer-sized voids was observed, but CaO did not crystallize even after prolonged irradiation. Amorphous apatite crystallized to a coarse-grained polycrystalline assemblage of apatite crystallites at 85–200 keV. Increasing the beam current through the sample caused the formation of fine-grained cubic CaO, and the crystallization of apatite was not observed, even at high doses. In each case, many beam-induced bubbles formed and were typically larger at the edge of the beam. Thermal annealing at 450 °C resulted in epitaxial crystallization from the thick portions of the TEM foil and resulted in a single crystal with a high defect density. Electron-beam irradiations at 300 °C confirmed that the difference in microstructural evolution as a function of current density is driven by dose-rate effects. In fact, temperature and dose rate are competing effects in the precipitation of CaO.

INTRODUCTION

Understanding the effects of radiation on apatite [$Ca_5(PO)_4F$ = fluorapatite, $Ca_5(PO_4)_3OH$ = hydroxyapatite] has several important applications. First, apatite can be used to investigate the potential beneficial or harmful effects of ionizing radiation on bones and teeth (Brès et al. 1991, and references therein; Ji and Marquis 1991; Nicopoulos et al. 1995). Previous work on dental enamel showed that electron irradiation can induce mass loss from voids, outgrowths on crystal surfaces, and crystallization of the inorganic constituents of the non-crystalline dental matrix. Second, because of the relatively high U content (up to several hundred parts per million substituting for Ca), apatite is used widely in geochronology. The age and thermal history of portions of the Earth's crust can be determined from the abundance and annealing rate of the damage tracks caused by the fission of ^{238}U (Carlson 1990; Green et al. 1989; Grivet et al. 1993; Hurford and Green 1982; Lutz and Omar 1991). A knowledge of the damage-production processes and annealing kinetics (thermal and radiation-enhanced) is essential to determine correct ages. Finally, apatite-structure silicates, often containing large amounts of P, are actinide-bearing constituents of simulated multiphase ceramic nuclear waste forms (Ewing et al. 1995; Wang et al. 1994a; Weber 1983). The actual chemical formula of nuclear waste apatite is $Ca_{4-x}Ln_{6+x}(SiO_4)_{6-y}(PO_4)_yO_2$, (Ln = lanthanides), where actinides readily substitute for lanthanides in the structure. Under these circumstances apatite may receive a high radiation dose because of α-decay events as well as β-particle irradiation over long time spans. As such, a detailed understanding of irradiation effects in apatite is clearly necessary. In this paper we document the effects of low energy (85 to 200 keV) electron irradiation on naturally occurring amorphous and crystalline apatite.

Electron- or ion-irradiation-induced segregation in crystalline materials was previously documented in alloys (Lam et al. 1987; Sorescu et al. 1995; Wiedersich 1986; Wollenberger 1994), although similar effects in minerals have been rarely reported. However, natural apatite undergoes extensive void formation followed by the precipitation of cubic CaO under a 200 keV electron irradiation (Cameron et al. 1992). Similar phase changes were observed in hydroxyapatite under electron irradiation, in which the following stoichiometrically balanced reactions were proposed (Ji and Marquis 1991, and references therein):

$$2Ca_5(PO_4)_3(OH) \rightarrow 3Ca_3(PO_4)_2 + CaO + H_2O \quad (1)$$

$$2Ca_5(PO_4)_3(OH) \rightarrow 2Ca_3(PO_4)_2 + Ca_4P_2O_9 + H_2O \quad (2)$$

Solid phase epitaxial recrystallization (SPE) of surface or buried amorphous layers in semiconductors and insulating ceramics as a result of electron irradiation is also well documented. Almost all of this work was done on silicon because of the importance of these recrystallization processes in the semiconductor industry, particularly

* Present address: Department of Nuclear Engineering and Radiological Sciences, The University of Michigan, Ann Arbor, Michigan 48109, U.S.A.

in very large scale integration technologies (Corticelli et al. 1990; Lulli and Merli 1993; Lulli et al. 1988; Lulli et al. 1987). Electron-irradiation-induced annealing of isolated damage cascades in Si, Ge, GeAs, and GaP occurred over a range of electron energies (Jencic and Robertson 1996; Jencic et al. 1995).

The mechanism for electron-irradiation-induced SPE of buried amorphous layers in semiconductors and in insulating ceramics is apparently material dependent. Suggested processes include enhanced defect mobility resulting from elastic interactions (Corticelli et al. 1990; Lulli and Merli 1993; Lulli et al. 1988; Lulli et al. 1987), ionization processes involving the breaking or rearrangement of unstable bonds (Jencic and Robertson 1996; Jencic et al. 1995; Spaepen and Turnbull 1982), and beam heating (Ewing and Headley 1983; Weber and Matzke 1986; Weber et al. 1986; Weber et al. 1985). For example, Lulli and coworkers found that silicon could not be induced to recrystallize epitaxially at beam energies lower that the displacement energy (E_d), suggesting an elastic-collision-driven recrystallization process, but Jencic et al. (1995) and Jencic and Robertson (1996) found the SPE process to be enhanced at these low energies for Si, Ge, GaP, and GaAs, indicative of an inelastic or ionization process. The crystallization of zircon under electron irradiation may be caused in part by electron-beam heating (Meldrum et al. 1997a).

More recently, electron-irradiation-induced nucleation and growth in amorphous monazite- and zircon-structure orthophosphates induced by 80 to 300 keV electron irradiation has been observed (Meldrum et al. 1997a). Crystallization was induced over a wide range of temperatures and beam energies and was attributed dominantly to an ionization process involving the breaking and rearranging of individual bonds under electron irradiation. Crystallization was induced at relatively low doses ($\sim 10^{20}$ cm^{-2}), and it was suggested that other materials, particularly orthophosphates, may be expected to show a similar effect. In the monazite- and zircon-structure orthophosphates, no phase segregation occurred; that is, the crystalline materials had the same stoichiometry as the initially amorphous materials.

Experimental methods

Single crystals of apatite from Ontario, Canada, were sectioned in random orientations and were chemically analyzed using a JEOL733 electron microprobe. The microprobe was operated at an accelerating voltage of 15 keV and the beam current was 20 nA. The beam diameter was approximately 1 μm. All elements were determined by wavelength dispersive spectrometry (WDS) using the Taylor apatite standard. Data were reduced by the ZAF-4 correction technique by using Oxford GENIE microprobe automation and data-analysis software.

The samples were hand polished and thinned to perforation using 4 keV Ar ions. Several samples were then irradiated in the IVEM-Tandem Facility at Argonne National Laboratory. This facility consists of a Hitachi H9000NAR intermediate-voltage electron microscope interfaced to a 400 keV ion accelerator. Samples were irradiated by Kr^{2+} ions accelerated through a potential difference of 400 kV (resulting in 800 keV doubly charged ions impinging on the sample) and were monitored in-situ during irradiation. The critical amorphization dose at room temperature was 2.9×10^{14} ions/cm^2, on the basis of the absence of electron-diffraction maxima. Samples were subsequently irradiated to double this dose to ensure complete amorphization.

Both the ion-beam–amorphized and original crystalline samples were then irradiated in JEOL 2000FX and JEOL 2010 transmission electron microscopes. The JEOL 2000FX has separate Gatan heating and cooling stages. Each stage has a Faraday cup. High-resolution images were obtained on the JEOL 2010 using a slow-scan digital camera. Electron dosimetry was monitored on the 2000FX by using the current readings from the Faraday cup. The current was measured before and after irradiation to confirm a constant dose rate. The beam area was obtained by photographing and digitally analyzing the beam profile. The crystallization dose was obtained by dividing the current readings from the Faraday cup by the beam area and multiplying by the observed crystallization time. Unless otherwise specified, all irradiations were done using an accelerating voltage of 200 keV and a current density of 1.6 A/cm^2 (low-current density conditions) or 16 A/cm^2 (high-current density conditions). Electron irradiation-induced phase changes were determined by monitoring the electron-diffraction patterns and the corresponding bright and dark field images by which crystallite growth or decomposition could be clearly observed. All photographs were taken by using 200 keV irradiations, although the beam current density was allowed to vary if necessary for optimum image quality.

Results

Electron microprobe analysis

Several analyses were taken along a traverse of the section, from edge to edge of the crystal, to determine the extent of chemical zoning. WDS analysis showed the apatite to have the end-member fluorine composition, with no detectable Cl on the anion site. Chemical zoning was not observed. Chemical variation in the sample was found to be minor (< 2 wt% of the total for all elements). Minor amounts of Fe and Mn were detected. Lanthanides and actinides were not determined. The stoichiometry was determined by normalization to 12 O atoms. The average chemical formula of this apatite is therefore $Ca_{4.99}P_{2.95}O_{12}F_{1.05}$ and the corresponding weight percents of the oxides are given in Table 1. The composition of this apatite is similar to the Durango apatite studied by Cameron et al. (1992) and is typical of natural apatite compositions.

Electron irradiation of crystalline apatite

Crystalline apatite undergoes several microstructural changes with progressing electron irradiation. Using a

TABLE 1. Chemical composition of the Ontario apatite used in this study

Oxide	Wt%	σ
CaO	54.2	0.23
MgO	<0.01	—
MnO	<0.01	—
FeO	0.02	0.01
P_2O_5	41.0	0.33
Cl	<0.02	—
F	4.1	0.05
Total	99.32	0.50

Notes: The values given are the average for 20 analyses representing a traverse across a single grain. Chemical variations were found to be minor. The standard deviations are given in the last column.

current density of 1.6 A/cm^2, small irregular regions of light contrast form almost immediately, as shown in the high resolution TEM images (Fig. 1). Cameron et al. (1992) observed similar structures in electron-irradiated apatite and on the basis of their shape suggested that they were voids, as opposed to bubbles or surface pits. Electron microscopy techniques were unable to distinguish unambiguously whether these were actually voids (empty) or bubbles (gas filled) and are termed voids to be consistent with previous work (Cameron et al. 1992) and to distinguish these from the larger ''bubbles'' that were observed to form in the amorphous apatite. The voids formed so rapidly that obtaining a void-free image was exceedingly difficult. Measurement of 100 of these voids gave an average diameter of 5 nm, with the largest having a diameter of 10 nm. Structural or chemical changes in the remaining crystalline apatite were not detected by TEM, despite the possible loss of volatile elements to the voids. With continued irradiation, using a high current density, the voids stabilized, and no further microstructural evolution was observed after 20 min of irradiation.

Focusing the beam on a region of the sample for several minutes induced the precipitation of fine-grained randomly oriented crystallites of cubic CaO, which were identified on the basis of the characteristic polycrystalline rings that developed in the electron-diffraction pattern (Fig. 1). The precipitation of CaO was so slow that in no case was the sample completely converted. In all cases at least 50% of the sample (on the basis of electron-diffraction patterns) was still crystalline apatite.

Electron irradiation of amorphous apatite: Low current-density conditions

Samples of ion-beam-amorphized apatite were initially checked by EDS in the TEM to determine whether there were any consistent compositional changes as a result of the Kr^{2+} irradiation. The current density was kept low (< 0.05 A/cm^2) during EDS analysis to ensure that electron-irradiation-induced microstructural changes were kept to a minimum. Consistent with calculations from the Monte Carlo computer code transport and range of ions in matter (TRIM) version 96.01 (Ziegler 1996), which indicate a total implanted concentration of less than 1 atom%, the amount of implanted Kr was below detection limits.

The initial response of the amorphous material to irradiation in each case was to produce a multitude of small bubbles (Fig. 2). These are distinguished from the defects formed in the crystalline material on the basis of their large size (up to 200 nm) and bubblelike appearance. Physically there may be no difference between the bubbles and the voids, but we retain this terminology to distinguish between the results for the irradiations of crystalline and amorphous apatite. The largest of these bubbles typically formed a ring delineating the edge of the electron beam (Fig. 2) and were occasionally observed to coagulate (Fig. 3). EDS analysis of these structures suggested a composition enriched in phosphorous relative to the amorphous matrix (Fig. 4).

Subsequent to the initial bubble formation, the amorphous apatite was induced to crystallize to an assemblage of randomly oriented micrometer-sized crystallites after several minutes of irradiation at 200 keV (Fig. 2). After the initial formation of several random nuclei in Figure

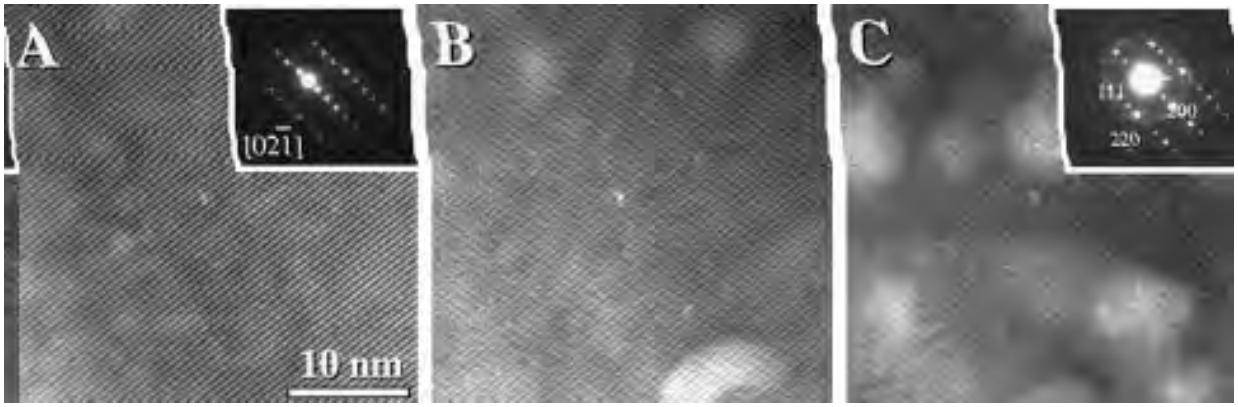

FIGURE 1. The formation of voids from electron irradiation in crystalline fluorapatite. The beam current density was 16 A/cm^2, using 200 keV electrons. The irradiation times were: (**A**) less than 10 s, (**B**) 1 min, and (**C**) 5 min. The corresponding electron-diffraction patterns are shown as insets. Polycrystalline rings giving the characteristic *d*-spacing of cubic CaO are evident in (**C**).

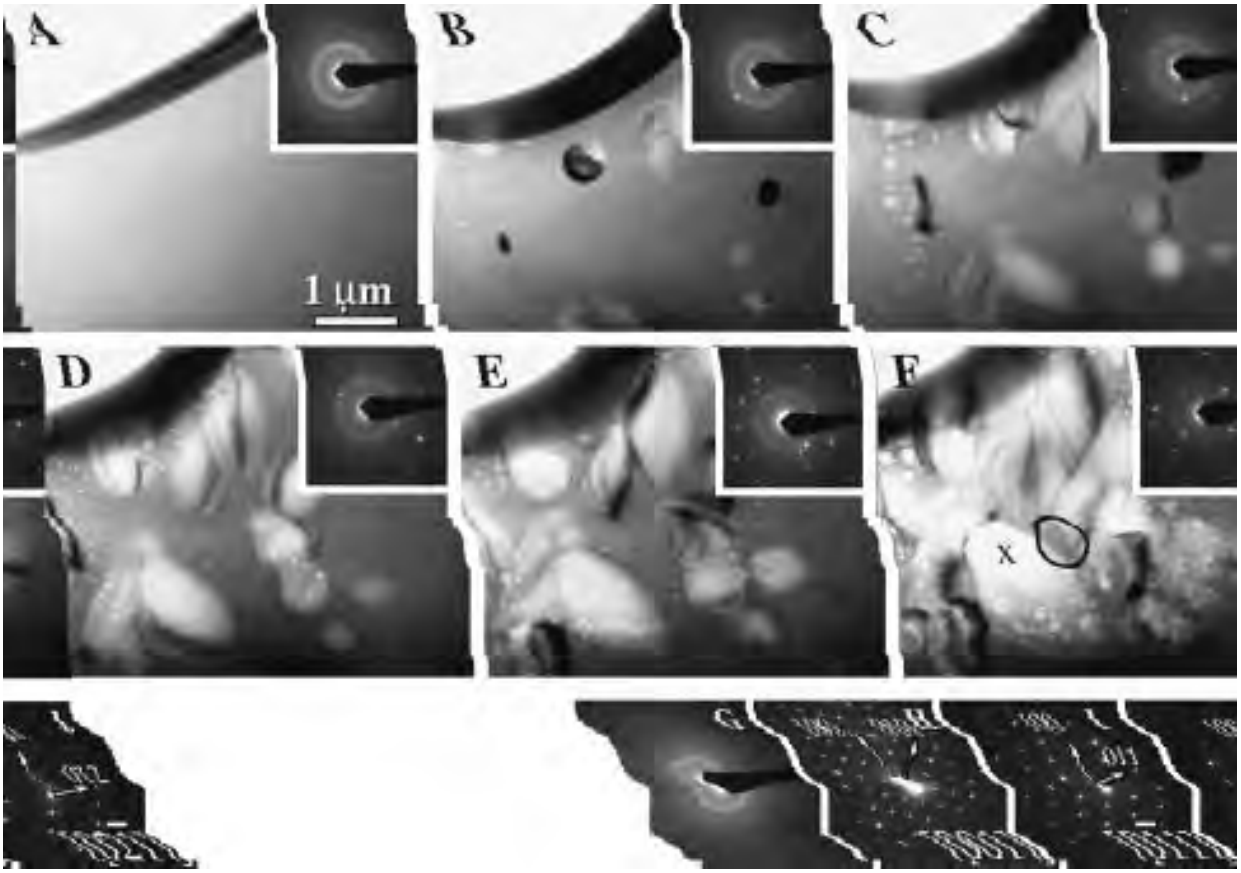

FIGURE 2. Room-temperature crystallization of amorphous apatite, using 200 keV electrons (J = 1.6 A/cm^2). The irradiation and image recording were done under the same beam conditions. The corresponding electron-diffraction patterns are shown in the insets. The area used for electron diffraction is bounded by the ring of bubbles and included all of the crystallites. An electron-diffraction pattern from the circular area marked in panel (**F**) is given in panel (**G**) and shows that the material is mostly amorphous at this grain-boundary location. Panels (**H**), (**I**), and (**J**) are single-crystallite selected-area electron-diffraction patterns from the crystallite marked by the ''X'' in panel (**F**), and confirm the apatite structure. The arrows were lengthened to point to the higher order spots (e.g., 200 instead of 100) for reasons of clarity.

2B, the nucleation process essentially ceased, and the crystals grew epitaxially. In Figure 2F the largest crystallite has a diameter of almost 2 μm. A ring of larger bubbles is evident at the perimeter of the crystallized area, the largest of which has a diameter of approximately 200 nm. The crystallization time was estimated by monitoring the electron-diffraction patterns and was taken to be the time at which the diffraction pattern showed only crystalline diffraction maxima (complete disappearance of the amorphous rings). These measurements were repeated four to five times to determine the experimental error (hence the 10% error bars). Some amorphous material was observed to remain along the grain boundaries, but this was not volumetrically large enough to be visible in the electron-diffraction patterns from the bulk area shown in the insets of Figure 2.

To minimize sample thickness effects, all electron-dose measurements were done at the thickest region from which an electron-diffraction pattern could be obtained, as described by others (Wang and Ewing 1992; Wang et al. 1994b). Amorphous apatite crystallized at a dose of 4.3×10^{21} cm^{-2} at room temperature. Lowering the current density to 0.3 A/cm^2 did not change the crystallization dose within experimental error (Table 1). Some amorphous material remained along the grain boundaries (Fig. 2) that could not be induced to crystallize even after prolonged irradiation.

The crystallites grew large enough that single-crystal electron-diffraction patterns could be obtained, unequivocally confirming the apatite structure (Fig. 2). Because of the large number of Ca-O-P phases, in many cases having similar lattice parameters, several zone axes were used to verify this identification. Further irradiation of these crystallites by using a high current density (16 A/cm^2) induced CaO precipitation, exactly as documented above for the electron irradiation of the crystalline samples.

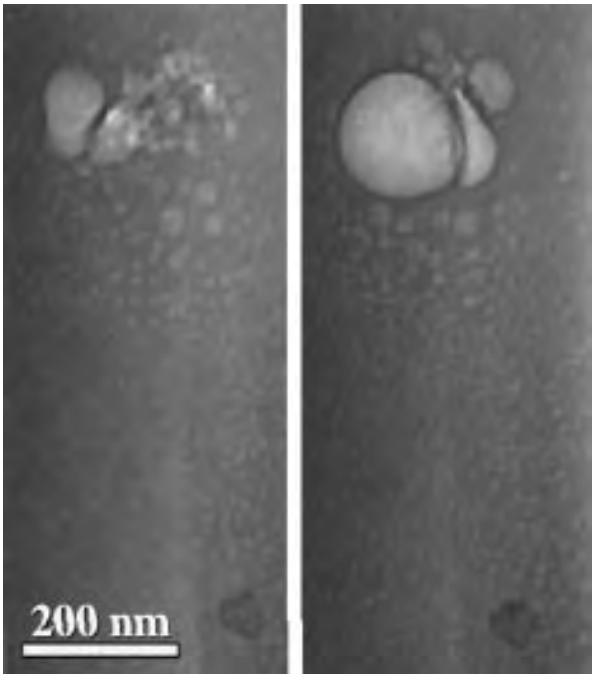

FIGURE 3. Coagulation of two large bubbles. This behavior suggests that the bubbles may be gas-filled.

The crystallites were chemically homogeneous on the scale of the electron beam (minimum beam diameter for EDS = 10 nm). Figure 4 shows a set of EDS spectra for the pristine (unirradiated) apatite, the ion-beam-amorphized material, the electron-beam crystallized apatite, and for a large bubble. The spectra from the amorphous material and the recrystallized region were from the same location on the sample (thus precluding thickness effects). Analysis of the large crystallites showed that they are chemically indistinguishable by EDS from the original crystalline apatite. The Ca-O-P ratio appeared to remain relatively constant in the pristine apatite, the ion-beam–amorphized material, and the electron-beam recrystallized apatite, suggesting that chemical changes on the scale of the electron beam, if any, are minor.

To investigate the process responsible for crystallization of amorphous apatite, irradiations were performed using beam energies ranging from 85 to 200 keV. The beam current densities for these irradiations are given in Table 2. The crystallization dose increased from 85 to 175 keV, and then decreased between 175 and 200 keV (Fig. 5). No change in the crystallite morphology occurred because of beam energy. Amorphous material along the grain boundaries was also noted as in the case of the 200 keV irradiations. A subsequent focused-beam irradiation at 125 keV did not induce CaO formation, possibly because of the lower current density (~5 A/cm^2) from operating the electron microscope at a low accelerating voltage. The maximum obtainable current density of the microscope was used for the low-energy focused-beam irradiations.

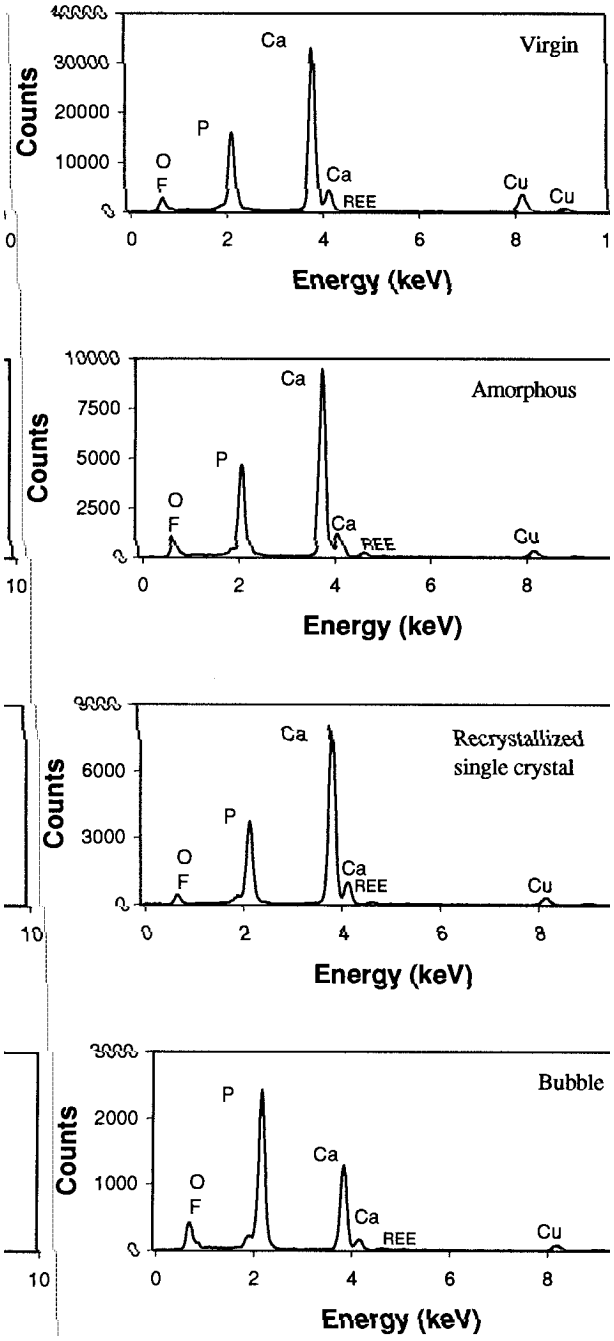

FIGURE 4. EDS spectra from the virgin apatite, the ion-beam–amorphized material, a crystallite formed by electron irradiation, and from a large bubble. The middle two spectra were from the same location on the sample, one before and one after electron irradiation. The large bubble is enriched in phosphorous in comparison with the amorphous material and the crystalline apatite.

Electron irradiation of amorphous apatite: High current-density conditions

Apatite crystallites could not be grown from the amorphous material, as described above, under a focused elec-

tron beam (J = 16 A/cm^2, E = 200 keV) even after 20 min of irradiation. Similar to the case of crystalline apatite, cubic CaO was observed to crystallize (Fig. 6), identified by its characteristic polycrystalline ring pattern. Precipitation of CaO could be induced after less than 60 s of irradiation, in comparison with the several minutes required for the crystalline starting material.

In addition to polycrystalline CaO, the material contained large bubbles and retained an amorphous component. Occasionally round or irregularly shaped bubbles as large as a 1 μm in diameter formed. The bubbles that formed as a result of the high-current-density irradiations were significantly larger than those formed under low-current-density conditions. The formation of bubbles occurred essentially instantaneously. Occasionally, relatively small apatite crystallites grew at the edge of the focused electron beam. Amorphous rings persisted in the diffraction pattern even at high doses (e.g., 1.2×10^{23} electrons/cm^2). Therefore, a 200 keV electron irradiation at 16 A/cm^2 apparently could not induce complete crystallization. These observations indicate that under high-current-density conditions, the crystallization of apatite is inhibited while that of CaO is strongly enhanced.

High-temperature electron irradiation of amorphous apatite

The 200 keV electron irradiations of amorphous apatite were repeated in the range 200–300 °C. Using a current density of 1.6 A/cm^2 (low-current-density conditions), nucleation and growth of crystalline apatite were faster by an order of magnitude (420 s at room temperature vs. ~60 s at 300 °C). Less bubble formation occurred before the material crystallized, although some bubbles were observed along the grain boundaries (Fig. 7). The resulting crystallites were smaller than those formed at room temperature, and no detectable amorphous component remained. Irradiation using a beam current of 16 A/cm^2 produced only crystalline apatite, not CaO, in contrast to the results of identical beam-current conditions at room temperature. Using a high current density, crystallization at 300 °C was very rapid: A few seconds at any location were sufficient to promote crystallization. Chemical changes resulting from the crystallization process were not detected by EDS analysis (Fig. 7).

Thermal annealing

To compare the temperature-driven microstructural evolution with that of the electron-beam-crystallized material, thermal anneals of the amorphous apatite were performed in the range of 300 to 500 °C. The material was initially heated to 300 °C and held at this temperature for 20 min. No crystallization was observed in this time, so the material was heated in 50 °C increments and held at each temperature for 20 min. At 450 °C, a crystallization edge advanced from the thick portions of the TEM foil into the electron-transparent regions. Because of the rapidity of electron-irradiation-induced crystallization at these high temperatures, it was not possible to obtain a sequence of images as in the previous experiments. The recrystallized material was a single crystal, although a high concentration of defect structures was observed (Fig. 8).

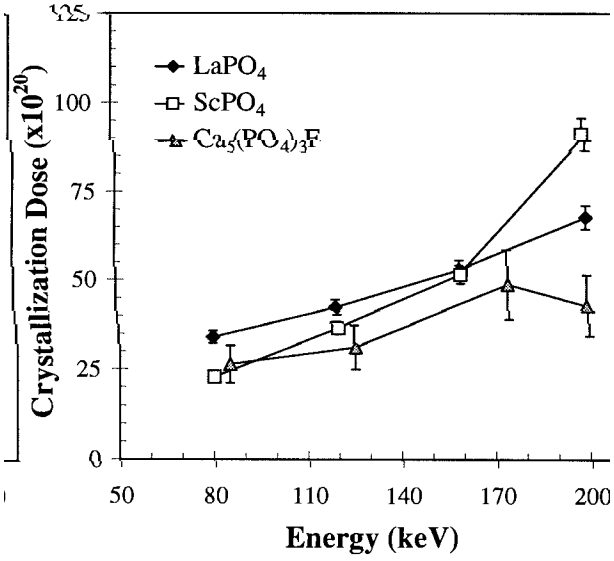

FIGURE 5. Energy vs. crystallization dose curves for apatite at room temperature (low current density from this study), compared with $LaPO_4$ and $ScPO_4$ (Meldrum et al. 1997a). The values for $LaPO_4$ are multiplied by a factor of ten to fit on the same scale. The latter two materials show a consistent increase in crystallization dose from 80 to 200 keV, but the dose for apatite peaks at approximately 175 keV and subsequently decreases at 200 keV. The error bars for $LaPO_4$ and $ScPO_4$ are ±5%, but those for apatite are ±10%. This is due to the greater difficulty in determining the crystallization dose for apatite because of the decreased rate of crystallization with time (no nucleation).

To determine the temperature for crystal nucleation, another sample was heated at a rate of ~20 °C/min. When the sample reached 520 °C the entire amorphous region crystallized nearly instantaneously. The crystallites were relatively large (up to several micrometers in diameter) and appeared to be randomly oriented, indicative of a true thermal-nucleation mechanism. No evidence for CaO precipitation was observed in the thermal annealing experiments.

DISCUSSION

Electron-beam heating

The possibility that beam heating may drive the crystallization process was extensively investigated in previous studies (e.g., Jencic and Robertson 1996; Jencic et al. 1995; Meldrum et al. 1997a). Thermally induced phase changes as a result of electron-beam heating can be used to estimate the beam-induced temperature rise (e.g., Curzon 1989; Sagaradze et al. 1994), but for materials where this is not possible several theoretical models have been developed to calculate the actual temperature rise (Cur-

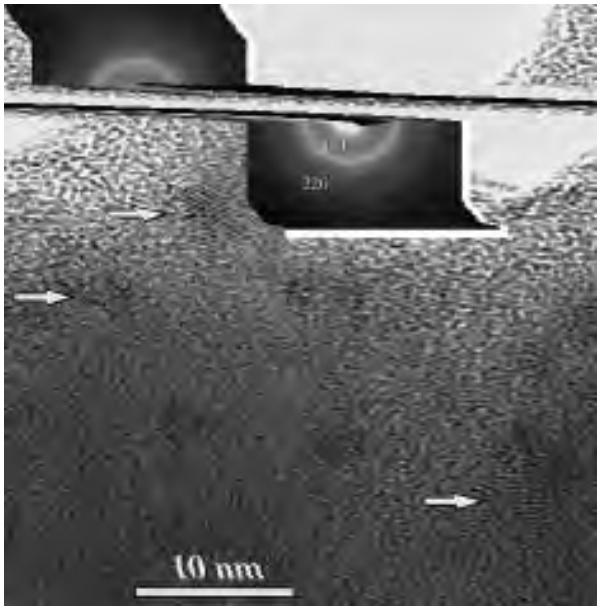

FIGURE 6. High-resolution image of CaO crystallization in amorphous apatite at room temperature (J = 16 A/cm^2, E = 200 keV). The irradiation time was 10 min. Several small CaO crystallites are marked with arrows. Even after prolonged irradiation, complete crystallization could not be induced; in fact, after 20 min, the crystallites were essentially the same size. Faint polycrystalline rings in the diffraction pattern confirmed the cubic CaO structure.

zon 1989; Fisher 1970; Liu et al. 1994). Of these, Fisher's model has been widely applied. According to this model, the temperature rise, ΔT, can be calculated according to the following equation:

$$\Delta T = \frac{I}{4\pi\kappa e}\left(\frac{\Delta E}{d}\right)\left(\gamma + 2\frac{b}{a}\right) \quad (3)$$

where e is the electron charge, γ is Euler's constant, a is the width of the Gaussian beam profile, b is the radius of the heat sink, κ is the thermal conductivity of the sample, I is the beam current, and ΔE is the energy loss per electron in a sample having a thickness, d. Jencic et al. (1995) demonstrated that Equation 3 can be solved for a non-Gaussian beam profile (overfocused second condenser lens, as in these experiments) and a sample containing a hole:

$$\Delta T = \frac{I}{\pi\kappa e}\left(\frac{\Delta E}{d}\right)\ln\frac{b}{r_0} \quad (4)$$

in which r_0 is the effective beam diameter. Under the assumption that the energy loss in the sample is small as compared with the initial energy, then the term $\Delta E/d$ is equal to dE/dx, the stopping power for electrons in the target of interest. The Bethe equation can be used to obtain dE/dx

$$-\frac{dE}{dx} = \frac{4\pi e^4 n}{mc^2\beta^2}\left[\ln\frac{mc^2\tau\sqrt{\tau+2}}{\sqrt{2}I} + F(\beta)\right] \quad (5)$$

in which e is the electron charge, n is the target electron density, m is the electron rest mass, c is the velocity of light in a vacuum, $\beta = v/c$ where v is the electron velocity, τ is the ratio E/mc^2 where E is the electron energy, I is the mean electron excitation energy of the target, and $F(\beta)$ can be calculated:

$$F(\beta) = \frac{1-\beta^2}{2} + \frac{1}{2(\tau+1)^2}\cdot\left[\frac{\tau^2}{8} - (2\tau+1)\ln 2\right]. \quad (6)$$

For a beam current corresponding to 1.6 A/cm^2 then dE/dx calculated from the Bethe equation for 200 keV electrons in apatite is 7.09 MeV/cm. The thermal conductivity of apatite is unknown, so the value used is the lowest available value for phosphate glass (0.75 W/m·K) (Lide 1996). A sample thickness of 100 nm was used to calculate the maximum temperature rise, although the diffraction patterns used to estimate the dose came from regions that are probably thicker than this (e.g., Wang and Ewing 1992; Wang et al. 1994a; Weber et al. 1994).

The calculated temperature increase, presented in Table 1 for all beam energies and currents used, varies from 13 to 70 °C for the low-current-density conditions, and was as high as 144 °C for the high-current-density conditions. These values are considered to be a maximum because (1) The maximum current reading was used in each case, (2) The thermal conductivity for crystalline apatite is very likely higher than the value used to calculate ΔT, and (3) A sample thickness of 100 nm was used in the calculations, which is probably thinner than the actual value.

Further evidence that electron-beam heating is not important includes (1) The total crystallization dose for the apatite crystallites was independent of dose rate (Table 1) in the low-dose-rate regime between 0.3 and 1.6 A/cm^2, within experimental error, and therefore is independent of temperature, (2) The phase assemblage for the high-current density experiments (e.g., CaO) is not that expected from heating alone (Fig. 9), and (3) If temperature alone were driving the microstructural evolution under electron irradiation, then the same phases would be expected to form under different irradiation conditions.

Epitaxial crystallization on relict crystallites?

Another possibility is that electron irradiation may induce epitaxial regrowth on ''invisible'' crystalline ''islands'' remaining in the amorphous matrix after ion-irradiation. Miller and Ewing (1992) demonstrated that at the critical amorphization dose for heavy-ion irradiation, more than 20 vol% crystalline material may still be undetectable in a high-resolution TEM image or the corresponding electron-diffraction pattern. This possibility is unlikely for the following reasons: (1) The materials were irradiated to a dose double that required for amorphization on the basis of the absence of electron-diffraction maxima. (2) The material crystallized to a randomly oriented phase assemblage, inconsistent with the single crystal starting material. Rotation of the crystallite islands after low-dose ion irradiation when reported is invariably small, for example in zircon (Weber et al. 1994). (3) The

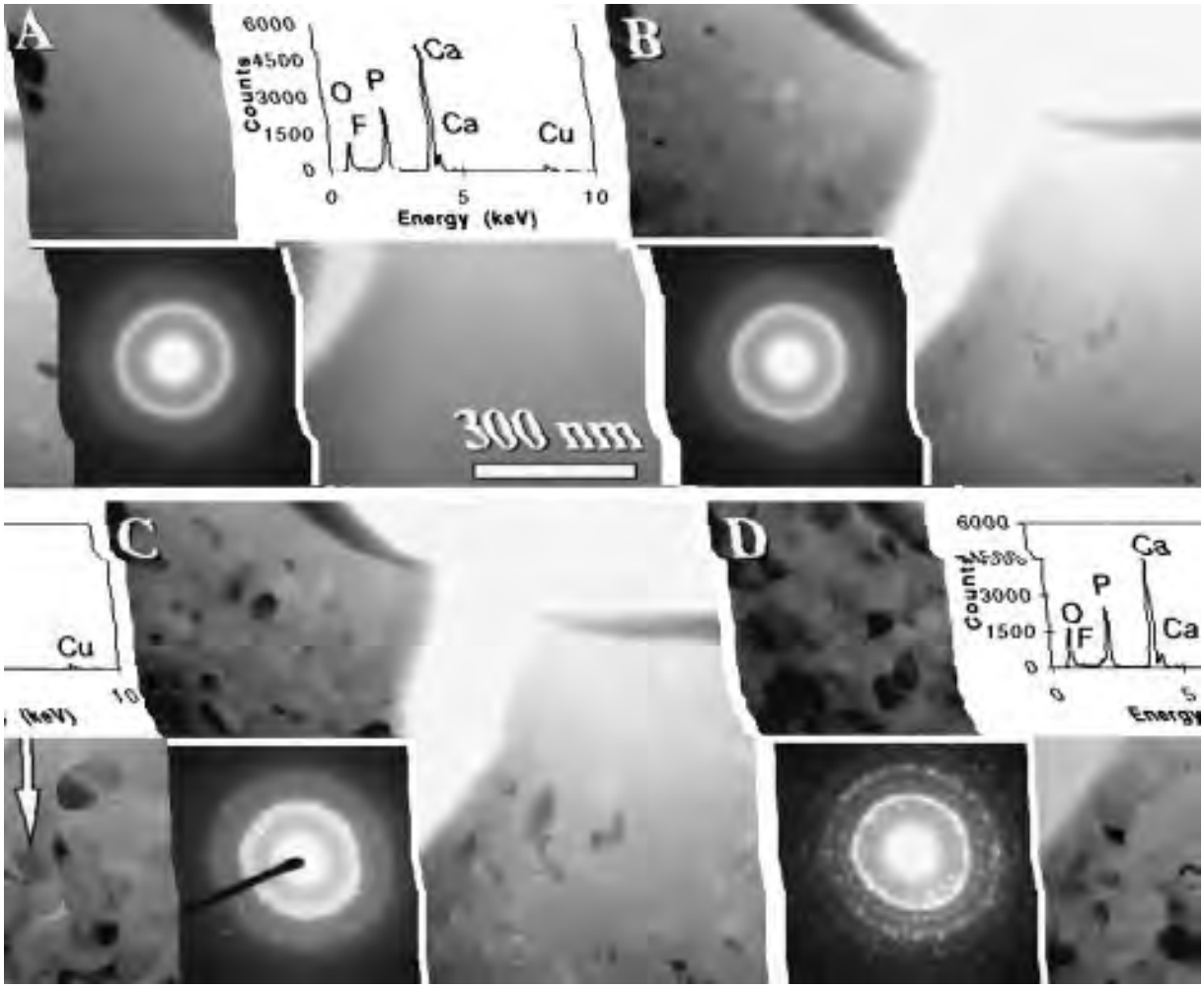

FIGURE 7. Crystallization sequence of amorphous apatite at 300 °C (J = 1.6 A/cm^2, E = 200 keV): (**A**) is less than 10 s, (**B**) is 25 s, (**C**) is 45 s, and (**D**) is 65 s. The microstructural development is markedly different from the room temperature irradiations (Fig. 2). In this case, the material has completely crystallized (no observable amorphous component remaining). After initial nucleation in (**B**), further nuclei continue to form in (**C**) at the same time that the previously existing crystallites continue to grow. This is different from Figure 2, in which the nucleation-process eventually stopped, and this accounts for the smaller size of the crystallites that form at high temperature. Bubble formation is drastically reduced, although in (**D**) some bubbles are evident along the grain boundaries. The diffraction patterns from the bulk-irradiated area, EDS spectra from the amorphous substrate, and a single crystal are shown in the insets. The photographs were obtained under the same beam conditions as the irradiation.

material crystallized to either apatite or cubic CaO, depending on the beam conditions. If relict apatite crystallites remained in the amorphous material after ion-irradiation, the material would be expected to crystallize only to apatite in all cases.

Energy dependence of the crystallization dose

The rate of crystallization, normalized to equivalent beam current, increased with decreasing electron energy below 175 keV, as demonstrated by an analysis of crystallization dose vs. beam energy (Fig. 5). The energy dependence of the crystallization dose for amorphous apatite suggests that ionization processes are important at energies lower than 175 keV. Similar to the lanthanide orthophosphates (Meldrum et al. 1997a), the crystallization dose at these energies scales roughly with the electronic stopping power, as calculated using the Bethe equation. The crystallization dose appears to peak at approximately 175 keV and subsequently decreases, suggesting that ballistic collisions may enhance the crystallization processes at high energies. The maximum energy transfer to a Ca atom by a 175 keV electron is 11 eV, and 27 eV to an O atom. Although the displacement energies for apatite are unknown, the maximum energy transfer from an electron to an O atom corresponds to the lower values of several insulating ceramics for which E_d

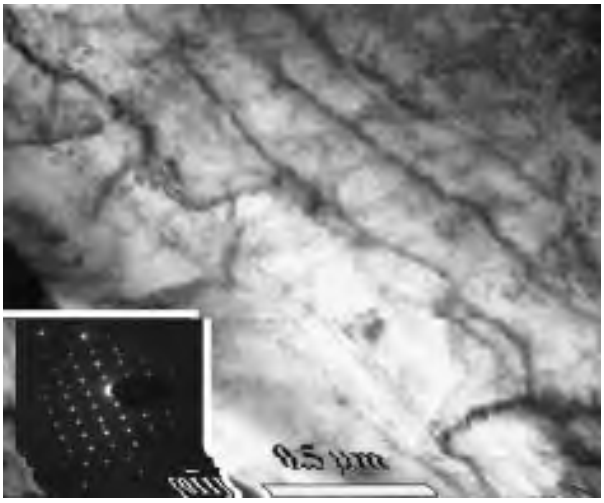

FIGURE 8. Results of thermal annealing at 450 °C. The material reverted to a highly defective single apatite crystal.

is known (Clinard and Hobbs 1986; Zinkle and Kinoshita 1997).

Thus, both electron excitation or ionization and nuclear interaction processes can cause the amorphous-to-crystalline phase transformation in apatite. Although there is no previous work on amorphous apatite, Brès et al. (1991) suggested that the microstructural changes observed in crystalline apatite as a result of electron irradiation were similarly driven by a combination of ionization and ballistic processes, as well as from the heating effects of the electron beam.

Bubble formation

The formation of voids or bubbles may alter the composition of the irradiated apatite. Although it is not possible to determine the composition in the bubbles completely independently from the surrounding material, the substance in the bubbles appears enriched in phosphorous in comparison with the amorphous starting material (Fig. 4). Void or bubble formation is fast under all conditions, although they grow at a more rapid rate in the amorphous matrix than in the crystalline matrix. In the crystalline material, the voids apparently stabilize after prolonged irradiation, so that no further evolution was observed. In the amorphous material, the bubbles at the edge of the electron beam appear to grow larger than those formed in the center. In some cases the edge of the beam profile is in fact delineated by a ring of larger bubbles (Fig. 2). These defects grew much larger in the amorphous material than in the crystalline apatite, possibly associated with more rapid diffusion in the amorphous substrate.

Precipitation of CaO

The effect of irradiating the amorphous material with a high-current density vs. a low-current density was to inhibit the crystallization of apatite and to enhance that of CaO. Some apatite was observed occasionally crystal-

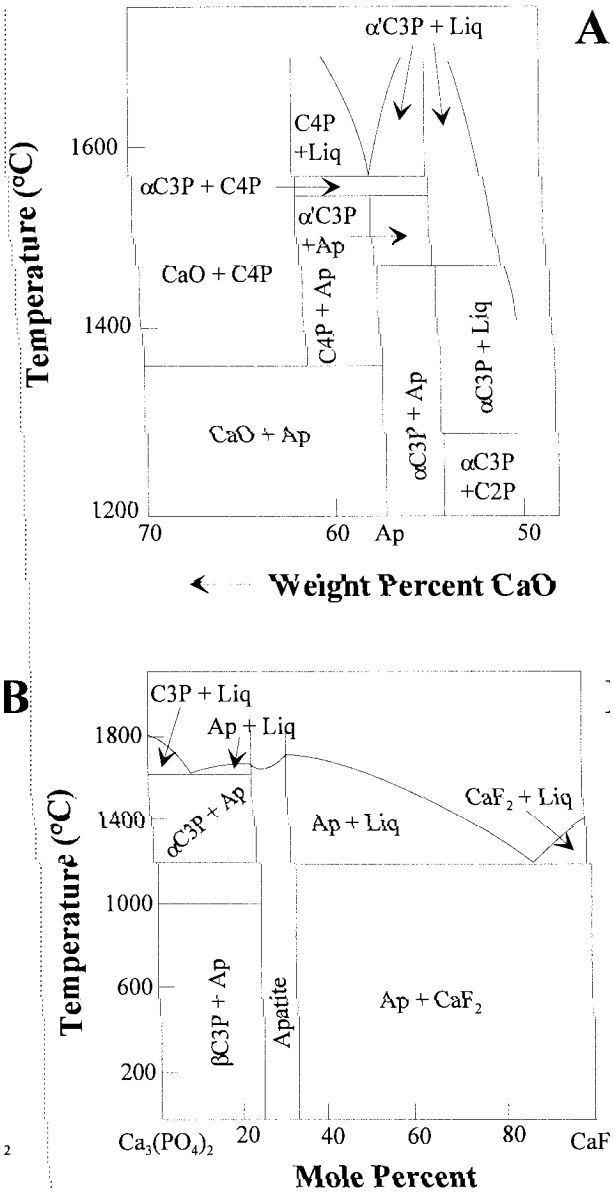

FIGURE 9. Phase diagrams for hydroxyapatite (**A**) and fluorapatite (**B**), modified after Roth et al. (1983). In (**B**) there is a solid solution from ~25 to 33 mol% CaF_2. C3P = $Ca_3(PO_4)_2$; C4P = $Ca_4P_2O_9$; C2P = $Ca_2P_2O_7$; and Ap = apatite.

lizing at the edge of the electron beam; however, this is probably related to the current drop-off at the beam edges. The random orientation and small size of the CaO crystallites formed under high-current-density conditions are consistent with homogeneous nucleation. These results could be interpreted to suggest that precipitation of CaO is dominantly temperature driven; whereas, crystallization of apatite is caused by the electron beam–solid interactions. Similarly, the formation of CaO in the crystalline starting material could be associated with the temperature rise caused by the focused electron beam. However, according to the phase diagram for hydroxyapatite

TABLE 2. Calculated crystallization dose and temperature rise for the electron irradiation of amorphous apatite

Energy (keV)	Time (s)	Current (nA)	Beam diameter (cm)	Beam area (cm^2)	Current density (A/cm^2)	Dose rate ($cm^{-2}s^{-1}$)	Crystallization dose (cm^{-2})	Temperature rise (°C)
200	420	53.4	0.000 204	3.27E−08	1.63	1.02E+19	4.28E+21	69
200	2430	9.9	0.000 204	3.27E−08	0.30	1.89E+18	4.59E+21	13
175	510	50.0	0.000 204	3.27E−08	1.53	9.56E+18	4.87E+21	69
125	660	24.6	0.000 204	3.27E−08	0.75	4.70E+18	3.10E+21	41
85	900	15.3	0.000 204	3.27E−08	0.47	2.92E+18	2.63E+21	16
200*	1200	54.3	0.000 065	3.32E−09	16.36	1.02E+20	1.23E+23	144

Notes: The crystallization dose is the same using a beam current of 1.63 A/cm^2 as for 0.30 A/cm^2, within 10% experimental error.
* High-current-density irradiation, in which crystallization was not fully accomplished, affects this whole row.

(Roth et al. 1983: Fig. 9a), Reaction 2, given above, is expected to occur: That is, CaO is not expected to crystallize as a result of the temperature increase alone. In the case of fluorapatite, the relevant phase diagram (Roth et al. 1983: Fig. 9b) shows that the material is expected to melt congruently to a liquid at approximately 1600 °C, again inconsistent with the formation of CaO. Thus, the precipitation of CaO is not temperature driven, despite the relatively high calculated values of ΔT for the high-current-density case (Table 2).

The reason for the pronounced difference in microstructural evolution when using a high-current density could be a combination of beam heating and electronic interactions, or could be a result of dose-rate effects. To test the first hypothesis, amorphous samples were irradiated at temperatures up to 300 °C in the TEM. CaO might then be expected to crystallize under a lower current density. The results showed that the crystallization was faster in all cases, but only apatite could be induced to form regardless of the beam current. Thus, the precipitation of CaO is driven by the high dose rate and is in fact reduced by the effect of increased temperature.

Previously, the formation of CaO from crystalline apatite was thought to depend on electron dose, not dose rate. After a critical dose, CaO was thought to crystallize independent of current density. To our knowledge, in all cases in which the beam conditions were specified, a focused beam was used to crystallize CaO, particularly in fluorapatite. Lower beam currents were thought similarly to induce precipitation of CaO, not observed, however, because of the long times required. This work shows that in fluorapatite, CaO does not form, either from the crystalline or amorphous starting materials, regardless of dose as long as the dose rate is low.

Atomistically, the dose-rate effect is difficult to determine by these methods. Apparently, stabilization of CaO requires the simultaneous interaction of more than one electron in the affected area, or in rapid succession, such that the effects of the previous electrons have not yet stabilized. The effect of increasing the temperature is to shorten this stabilization time, so that apatite crystallizes instead of CaO under identical beam-current conditions. Thus, dose rate and temperature are competing effects in the precipitation of CaO. Presumably, once CaO nucleates, the composition of the remaining material is stoichiometrically incorrect for the crystallization of apatite. In any case, the precipitation of CaO must involve bond breaking. One interesting interpretation of these results is that the formation of CaO through bond-breaking processes is driven primarily by ballistic collisions between the electrons and the Ca atoms or their neighboring O atoms; whereas, the crystallization of apatite from the amorphous matrix is dominantly a result of ionization processes, possibly explaining why CaO was not observed to form in the low-beam-energy irradiations.

Nucleation of apatite

Under low-current density conditions, crystallites apparently do not nucleate everywhere, as seen in $LaPO_4$ (Meldrum et al. 1997a). Instead, a few crystalline nuclei form and then grow epitaxially: Further nucleation in the amorphous matrix rarely occurs. The large size of the apatite crystals grown under low-current density conditions at room temperature suggests a heterogeneous nucleation mechanism. For example, the nucleation sites may be relict crystalline islands remaining after ion irradiation (unlikely for reasons discussed above), particular defect structures at which nucleation is favorable, strain centers, or could be a result of chemical inhomogeneities. Of these possibilities, the last is considered the most likely because the formation of voids and bubbles suggests the presence of chemical variability. Nucleation at certain defect clusters is unlikely because these clusters would have to be exceedingly rare to occur in isolated regions separated by several micrometers.

However, the results of the irradiations conducted at 300 °C are different in that the crystallites were smaller and more abundant and more characteristic of a homogeneous nucleation process. Also, the crystallization sequence was different because random nucleation continued to occur at a rapid rate as the previously existing nuclei continued to grow (Fig. 7). Of particular importance is that the bubbles were rare in comparison with those observed in the room-temperature experiments (compare Figures 2 and 7). At high temperature, nucleation from the electron beam was so fast that bubbles had little time to form. This strongly suggests that the reduced rate of nucleation as a function of time observed in the room-temperature experiments results from the change in the bulk chemistry of the solid because of bubble for-

mation. Thus, the nucleation and growth pattern is not a result of heterogeneous nucleation, but occurs because the chemistry of the amorphous matrix becomes non-stoichiometric for the nucleation of apatite.

The crystallization of the amorphous material is apparently easily accomplished in materials containing isolated PO_4 tetrahedra (Meldrum et al. 1997b). This ease has been attributed to the possibility of a glass-like coordination of the phosphate tetrahedra in the amorphous matrix; that is, each tetrahedron is only bonded through three of its four O atoms. Thus, rotation and reorganization of the tetrahedra under irradiation is easier, in comparison with isostructural silicate analogues in which all four O atoms act as bridges to adjacent coordination polyhedra. The crystallization of apatite in these experiments is consistent with this proposal and is consistent with the generally low diffusion-driven irradiation-enhanced activation energies for annealing in the orthophosphates (Meldrum et al. 1997b; Wang et al. 1994a).

Stoichiometric considerations

Previous researchers suggested that void formation in the crystalline hydroxyapatite matrix may result from the volatilized H_2O in Reactions 1 and 2 (Brès et al. 1991; Ji and Marquis 1991). The other calcium phosphate phases were identified as crystallized from hydroxyapatite by single-crystal electron-diffraction patterns (Nicopoulos et al. 1995). However, in this case the results are different because apatite [not $Ca_3(PO_4)_2$] clearly remains as the only Ca-O-P crystalline component (with some CaO eventually crystallizing at high dose) in the initially crystalline samples. Apart from apatite, no other crystalline phosphate-bearing phases were identified. Moreover, if those phases represented the stable assemblage, one expects them to crystallize from the amorphous matrix. This was not observed. Thus, a balanced equation (e.g., Eq. 1 or Eq. 2) does not seem to be applicable to these results. Additionally, in the case of F-bearing apatite, some of the material may remain amorphous along the grain boundaries (Fig. 2).

In the case of irradiation of the crystalline fluorapatite, previously only CaO, voids, and remaining apatite were identified (Cameron et al. 1992). However, this phase assemblage is not stoichiometrically balanced if the voids contain F, as suggested by Cameron et al. (1992). This imbalance suggests that some component of the irradiated apatite was not detected. This undetected material could be in the voids or could be amorphized by the electron beam. Both possibilities are supported by the present results, which show that under high-current density conditions not all of the material can be induced to crystallize and that the bubbles appear to contain a P-rich compound.

Conclusions

Apatite has a strong tendency to crystallize under electron irradiation. The crystallization products depend on the dose rate and on the ambient temperature. These results suggest that beta-decay in natural or nuclear-waste-loaded apatite has the potential to inhibit amorphization, contrary to the traditional understanding that beta decay may weakly enhance the damage-accumulation process. This enhanced defect recombination as a result of electron irradiation also has potential implications for the stability of apatite fission tracks, particularly in samples with a high radioelement concentration that may be subjected to a high beta-decay dose over geologic time.

Acknowledgments

The authors thank the staff at the HVEM-Tandem Facility at Argonne National Laboratory for their assistance with the ion irradiations. This manuscript was significantly improved as a result of critical reviews by Gordon Nord and an anonymous reviewer. Electron irradiations were performed under the supervision of Y.X. Guo at the University of New Mexico Electron Microbeam Facility. This work was supported by the Office of Basic Energy Sciences, DOE (grant no. DE-FG03-93ER45498). A.M. acknowledges financial support through a scholarship from les Fonds pour la Formation de Chercheurs et de l'Aide à la Recherche (FCAR, Québec). This work was also supported in part by Research Grant to A.M. from the Mineralogical Society of America.

References cited

Brès, E.F., Hutchison, J.L., Senger, B., Voegel, J.-C., and Frank, R.M. (1991) HREM study of irradiation damage in human dental enamel. Ultramicroscopy, 35, 305–322.

Cameron, M., Wang, L.M., Crowler, K.D., and Ewing, R.C. (1992) HRTEM observations on electron-irradiation damage in F-apatite. In G.W. Bailey, J. Bentley, and A. Small, Eds., Proceedings of the 50th Annual Meeting of the Electron Microscopy Society of America, p. 378. San Francisco Press, California.

Carlson, W.D. (1990) Mechanisms and kinetics of apatite fission-track annealing. American Mineralogist, 75, 1120–1139.

Clinard, F.W. and Hobbs, L.W. (1986) Radiation effects in non-metals. In R.A. Johnson and A.N. Orlov, Eds., Physics of Radiation Effects in Crystals, p. 387–472. Elsevier, Amsterdam.

Corticelli, F., Lulli, G., and Merli, P.G. (1990) Solid-phase epitaxy of implanted silicon at liquid nitrogen and room temperature induced by electron irradiation in the electron microscope. Philosophical Magazine Letters, 61, 101–106.

Curzon, A.E. (1989) The increase in temperature of a rectangular film when subjected to electron irradiation and/or high-temperature thermal irradiation. Journal of Physics D: Applied Physics, 22, 295–301.

Ewing, R.C. and Headley, T.J. (1983) Alpha-recoil damage in natural zirconolite ($CaZrTi_2O_7$). Journal of Nuclear Materials, 119, 102–109.

Ewing, R.C., Weber, W.J., and Clinard, F.W. (1995) Radiation effects in nuclear waste forms for high-level radioactive waste. Progress in Nuclear Energy 19, 63–127.

Fisher, S.B. (1970) On the temperature rise in electron irradiated foils. Radiation Effects, 5, 239–243.

Green, P.F., Duddy, I.R., Laslett, G.M., Hegarty, K.A., Gleadow, A.J.W., and Lovering, J.F. (1989) Thermal annealing of fission tracks in apatite. Chemical Geology, 79, 155–182.

Grivet, M., Rebetez, M., Ghouma, N.B., Chambaudet, A., Jonckheere, R., and Mars, M. (1993) Apatite fission-track age correction and thermal history analysis from projected track length distributions. Chemical Geology, 103, 157–169.

Hurford, A.J. and Green, P.F. (1982) A users guide to fission track dating calibration. Earth and Planetary Science Letters, 59, 343–354.

Jencic, I. and Robertson, I.M. (1996) Low-energy electron-beam induced regrowth of isolated amorphous zones in Si and Ge. Journal of Materials Research, 11, 2152–2157.

Jencic, I., Bench, M.W., and Robertson, I.M. (1995) Electron-beam-induced crystallization of isolated amorphous regions in Si, Ge, GaP, and GaAs. Journal of Applied Physics, 78, 974–982.

Ji, H.I. and Marquis, P.M. (1991) Modification of hydroxyapatite during transmission electron microscopy. Journal of Materials Science Letters, 10, 132–134.

Lam, N.Q., Okamoto, P.R., and Leaf, G.K. (1987) Formation of submicrometer metastable phase structures in alloys with focused electron or proton beams. Materials Research Society Symposium Proceedings, 74, 523–528.

Lide, D.R. Ed. (1996) CRC Handbook of Chemistry and Physics, 76th Edition. CRC Press, Boca Raton, Florida.

Liu, M., Xu L.Y., and Lin, X.Z. (1994) Heating effect of electron beam bombardment. Scanning, 16, 1–5.

Lulli, G. and Merli, P.G. (1993) Comparison of results and models of solid-phase epitaxial regrowth of implanted Si layers induced by electron- and ion-beam irradiation. Physical Review B, 47, 14023–14031.

Lulli, G., Merli, P.G., and Antisari, V. (1987) Solid phase epitaxy of amorphous silicon induced by electron irradiation at room temperature. Physical Review B, 36, 8038–8042.

Lulli, G., Merli, P.G., and Antisari, V. (1988) Solid phase epitaxy of implanted silicon by electron irradiation at room temperature. Materials Research Society Symposium Proceedings, 100, 375–380.

Lutz, T.M. and Omar, G. (1991) An inverse method of modeling thermal histories from apatite fission-track data. Earth and Planetary Science Letters, 104, 181–195.

Meldrum, A., Boatner, L.A., and Ewing, R.C. (1997a) Electron irradiation-induced nucleation and growth in amorphous $LaPO_4$, $ScPO_4$, and zircon. Journal of Materials Research, 12, 1816–1827.

Meldrum, A., Boatner, L.A., Wang, L.M., and Ewing, R.C. (1997b) Ion-Beam-Induced Amorphization of $LaPO_4$ and $ScPO_4$. Nuclear Instruments and Methods in Physics Research B (in press).

Miller, M.L. and Ewing, R.C. (1992) Image simulation of partially amorphous materials. Ultramicroscopy, 48, 203–237.

Nicopoulos, S., González-Calbet, J.M., Alonso, M.P., Gutierrez-Rios, M.T., de Frutos, M.I., and Vallet-Regi, M. (1995) Characterization by TEM of local crystalline changes during irradiation damage of hydroxyapatite compounds. Journal of Solid State Chemistry, 116, 265–274.

Roth, R.S., Negas, T., and Cook, L.P. (1983) Phase Diagrams for Ceramists, Volume 5, American Ceramic Society, Columbus, Ohio.

Sagaradze, V.V., Shabashov, V.A., and Arbuzov, V.L. (1994) Phase transformations in austenitic Fe-Ni and Fe-Ni-Ti alloys during low-temperature electron irradiation. Physics of Metals and Metallography, 78, 414–418.

Sorescu, M., Knobbe, E.T., and Barb, D. (1995) Evolution of phases and microstructure in $Fe_{81}B_{13.5}Si_{3.5}C_2$ metallic glass during electron-beam and pulsed-laser irradiation. Physical Review B, 51, 840–850.

Spaepen, F. and Turnbull, D. (1982) Crystallization processes. In J.M. Poate and J.W. Mayer, Eds., Laser Annealing of Semiconductors, p.15–42. Academic Press, NewYork.

Wang, L.M. and Ewing, R.C. (1992) Ion beam-induced amorphization of $(Mg,Fe)_2SiO_4$ olivine series: an in-situ transmission electron microscopy study. Materials Research Society Symposium Proceedings, 235, 333–338.

Wang, L.M., Cameron, M., Weber, W.J., Crowley, K.D., and Ewing, R.C. (1994a) In-situ observation of radiation induced amorphization of crystals with apatite structure. In P.W. Brown and B. Constantz, Eds., Hydroxyapatite and Related Materials, p. 243–249. CRC Press, London.

Wang, L.M., Gong, W.L., and Ewing, R.C. (1994b) Amorphization and dynamic recovery of A_2BO_4 structure types during 1.5 MeV krypton ion-beam irradiation. Materials Research Society Symposium Proceedings, 316, 247–252.

Weber, W.J. (1983) Radiation-induced swelling and amorphization in $Ca_2Nd_8(SiO_4)_6O_2$. Radiation Effects, 77, 295–308.

Weber, W.J. and Matzke, H. (1986) Effects of radiation on microstructure and fracture properties in $Ca_2Nd_8(SiO_4)_6O_2$. Materials Letters, 5, 9–15.

Weber, W.J., Wald, J.W., and Matzke, H. (1985) Self-radiation damage in $Gd_2Ti_2O_7$. Materials Letters, 3, 173–180.

Weber, W.J., Wald, J.W., and Matzke, H. (1986) Effects of self-radiation damage in Cm-doped $Gd_2Ti_2O_7$ and $CaZrTi_2O_7$. Journal of Nuclear Materials, 138 196–209.

Weber, W.J., Ewing, R.C., and Wang, L.M. (1994) The radiation-induced crystalline-to-amorphous transition in zircon. Journal of Materials Research, 9, 688–698.

Wiedersich, H. (1986) Phase stability and solute segregation during irradiation. In R.A. Johnson and A.N. Orlov, Eds., Physics of Radiation Effects in Crystals, p. 225–282. Elsevier, Amsterdam.

Wollenberger, H. (1994) Phase transformations under irradiation. Journal of Nuclear Materials, 216, 63–77.

Ziegler, J.F. (1996) TRIM Version 96.01. IBM-Research, Yorktown, New York.

Zinkle, S.J. and Kinoshita, C. (1997) Defect production in ceramics. Journal of Nuclear Materials, in press.

Manuscript received November 15, 1996
Manuscript accepted June 4, 1997